

Airborne Optical System for Remote Sensing of Ocean Waves

J. P. DUGAN

Areté Associates, Arlington, Virginia

G. J. FETZER AND J. BOWDEN

Areté Associates, Tucson, Arizona

G. J. FARRUGGIA, J. Z. WILLIAMS, C. C. PIOTROWSKI, AND K. VIERRA

Areté Associates, Arlington, Virginia

D. CAMPION

Areté Associates, Sherman Oaks, California

D. N. SITTER

Areté Associates, Tucson, Arizona

(Manuscript received 1 March 2000, in final form 9 October 2000)

ABSTRACT

A compact, turret-based optical system has been designed and constructed for passive imaging of ocean waves using a small aircraft. The purpose of the system is to collect time series of images, which are mapped to a common geodetic surface in order to extract the space–time characteristics of the waves. This is achieved by *staring* at a fixed geodetic location and by accurately measuring the imaging geometry. The system was designed to be compact and lightweight for future installation on an unmanned aerial vehicle and has been installed on a small, manned, single-engine aircraft for testing and experimentation. Initial tests have confirmed successful operation of the staring capability at moderate distances to a fixed target array on land and to the nearshore region with shoaling gravity waves. Images were mapped to a common reference frame on a geodetic surface at the mean ocean level, and a three-dimensional spectrum of the *space–time data cube* of the mapped image modulations exhibits the expected, well-resolved dispersion surface for surface gravity waves. This paper describes the data collection system, the processing procedures, and the preliminary results.

1. Introduction

The U.S. Naval Oceanographic Office has defined a strategic requirement for obtaining bathymetry surveys of large areas of the world's coastline. Unfortunately, present capabilities using survey ships and launches are extremely slow, and access to some coasts is restricted. The requirement may be partially satisfied through the use of airborne or satellite passive optics (Bierwirth et al. 1993) or airborne active optics (Lillycrop et al. 1996), which view the ocean bottom directly. However, these techniques require very clear water for depths of interest. Such clarity occurs at only a fraction of the geographic areas for which bathymetry surveys are desired.

Thus, alternative techniques for satisfying this requirement are needed.

One approach for estimating the coastal bathymetry at a useful level of accuracy is to develop a passive airborne optics system that remotely senses the surface gravity waves over a large area (on the order of a few square kilometers) and that extracts depth from the space–time behavior of the waves. This approach would use a passive sensor to image the surface waves by measuring their effect on the brightness distribution, with the space–time behavior of the measured radiance replicating the space–time behavior of the waves. Potentially, this approach could provide the average depth at intervals of perhaps 100 m at locations where the waves are long enough to feel the bottom. A system with this capability would provide a high rate of coverage combined with moderate resolution at a relatively low operating cost. In addition, the ability to obtain

Corresponding author address: Dr. John Dugan, Arété Associates, 1725 Jefferson Davis Highway, Crystal Square 2, Suite 703, Arlington, VA 22202.
E-mail: dugan@arete-dc.com

bathymetry data from a moderate standoff range is advantageous in military applications.

The primary goal of the development discussed here was to construct a prototype for demonstrating this capability. The system concept is an extension of ideas that were originally used operationally on aircraft during World War II and more recently on a limited research basis using land- or tower-based remote sensors. The fundamental basis of the approach is to utilize time series of ocean images to measure the surface wavelengths and speeds and to use the theoretical gravity wave dispersion relation to retrieve depth and currents. This is done by transforming 3D space-time wave image data into frequency-wavenumber (ω - κ) spectra, where the frequency ω is $2\pi/T$, where T is the period, and the wavenumber κ is $2\pi/\lambda$, where λ is the wavelength. The theoretical dispersion relation codifies the dependence of these spectra on the depth and currents over which the waves are traveling. The location of the low-frequency portion of the dispersion surface is sensitive to water depth, and the high frequency portion is sensitive to currents, thereby providing a technique for estimating both quantities. Depth and current velocity are retrieved by fitting the theoretical dispersion relation to the observed spectra. Simpler aspects of this technique were applied to aircraft photographic data for surveillance of defended beaches in World War II with some success (Seiwell 1947; Lundahl 1948). Back then, individual still photographs were used to estimate the depth by measuring the change in wavelength of narrowband swell as the waves passed from deep to shallow water. Alternatively, the speed of narrowband swell was estimated from two images closely spaced in time, and this was used with the dispersion relation to estimate the depth. These techniques had limitations, but were useful at the time, considering no other data were available.

Passive optical imagers have also been mounted on towers and used for estimating 2D wavenumber spectra (Barber 1949; Stilwell 1969) and 3D ω - κ spectra (Kasovich et al. 1972; Lubard et al. 1980). These imagers collect the radiance that is emitted and reflected at the surface. At modest grazing angles, the modulations in the radiance are dominated by the reflection of the sky radiance by the changing wave slopes (Walker 1994). Since the wavelengths of visible light are much shorter than the lengths of the waves on the surface, the reflection mechanism is mostly specular and the measured radiance modulations closely replicate the line-of-sight wave slope modulations. The precise magnitude of the radiance modulations depends upon the wave slopes and the radiance gradient of the background sky. The latter typically is not known in absolute units, so these measurements cannot be utilized to retrieve the actual wave slope magnitudes. However, this uncertainty in the actual slopes does not affect the temporal or spatial distribution of the modulating radiance, so the distribution of variance in spectral space is not affected at all. In

electrical engineering parlance, the *gain* factor in the modulation transfer function between these fields is unknown, but otherwise, the modulations are replicates. Thus, the ω - κ spectra that were calculated from the images in these previous investigations clearly resolved the dispersion relation of the waves that were present, and the dispersion surface was appropriately located for deep water gravity waves even though the spectral power could not be related quantitatively to wave slopes. In conclusion, it is clear that the radiance spectra replicate the wave slope spectra reasonably well even if the gain factor between them is not known.

In more recent years, Young et al. (1985) and Williams and Dugan (1997) among others have applied this technique to sequences of images from a land-based radar or video camera staring out over the water. In these cases, time series of the 1D or 2D spatial data were accumulated, and the 2D or 3D space-time datasets were Fourier transformed to determine the location of the wave dispersion surface. While this technique is useful for the region near the tower, it is limited to rather small area surveys by the difficulty of accurately mapping image data acquired at low grazing angles. Also, the wave information in imagery collected at low grazing angles can be severely distorted by registration errors due to finite wave heights (Chapman and Irani 1981). The limitations imposed by low grazing angle and small area coverage may be remedied by collecting imagery from an airborne platform, with the concomitant difficulty of mapping the changing scene to a common reference frame on the surface. Dugan et al. (1996) analyzed data collected at long range (~ 80 km) with an airborne infrared imaging system and achieved a preliminary level of success in performing this mapping and detecting the dispersion surface in the spectra of shoaling waves. Dugan (1997) also used these data to estimate the water depth, although the low grazing angle at which the data were collected ($\sim 8^\circ$) prevented the achievement of high accuracy. To the best of our knowledge, the approach of using passive optical imagery of surface waves collected from an airborne platform to obtain bathymetry and currents has not otherwise been utilized.

In an entirely different approach for estimating the geometry of nearshore bars, Holman and students (Lippmann and Holman 1989; Holland et al. 1997) have utilized video cameras on towers near the beach to obtain time-averaged images of the surf, and these have been useful in determining the location and morphology of the nearshore bar. In this case, the location of the bar is identified as the brightest region, which is associated with the Lambertian scattering of the foam on the surface. This technique could also be applied to imagery collected with an airborne system, thereby broadening the capability exhibited by these investigators to extended lengths of coastline.

With the above motivation, the primary goal of this development was to design and construct a camera sys-

tem on an airborne platform to provide both portability and moderate grazing angles. To be successful in this application, the system had to exhibit a number of specific characteristics. Accurate registration of the imagery was deemed most crucial, so that spatial and temporal aspects would be accurately separated and the derived data have appropriate characteristics for measuring the location of the dispersion surface in the resulting spectra. Adequate spatial resolution, field of view, dwell, and dynamic range were also identified as important elements, and a detailed discussion of the requirements and system components is provided in section 2. Given these characteristics, the data obtained by this system could potentially be used to estimate bathymetry and currents, as information on these parameters is encoded in the ω - κ luminance spectra. The directional properties of the waves are also contained in these luminance spectra, although the absolute spectral variance densities remain in units of radiance and not wave amplitudes. As such, they do not have the correct units for the directional spectrum of wave height, as noted previously. A second goal of this effort was to construct the system so that it could be used on small single-engine aircraft and ultimately moved to unmanned aerial vehicles (UAVs).

The design approach was to utilize a commercial off-the-shelf (COTS) turret-type positioner, digital framing camera, and integrated Global Positioning System/inertial measurement unit (GPS/IMU), with a computer-based data acquisition and control system. Attitude and position information are provided by the GPS/IMU, which was mounted within the turret rather than on the airframe. The control system uses this information, along with differential GPS corrections, to calculate the camera pointing direction and maintain the intended geodetic location of the aim point in proximity to the center of the image.

This system, called the Airborne Remote Optical Spotlight System (AROSS), was designed, constructed, and successfully flown on a small aircraft that operates as a UAV surrogate (Bluth et al. 1996). Its performance is currently being evaluated for the intended application. This paper provides an overview of its design, a verification of its staring capability, and preliminary results obtained from images of ocean waves. The system is described in section 2, the data processing procedures in section 3, and preliminary results in section 4.

2. System requirements and description

In order to use imagery of ocean waves to measure water currents and bathymetry, it is important to resolve waves of appropriate scales. These two parameters have conflicting requirements, since only the shortest waves are Doppler-shifted a significant amount by the currents, yet the water depth affects only the longer waves. This dependence is given by the surface gravity wave dispersion relation

$$\omega = [g\kappa \tanh(\kappa h)]^{1/2} + \kappa \cdot \mathbf{U}. \quad (1)$$

In this relation, g is the acceleration of gravity; h the water depth; \mathbf{U} the surface current vector; κ and κ the vector and scalar spatial wavenumbers, respectively; and ω the temporal frequency of any particular wave spectral component, with κ and ω as defined in section 1. Thus, a broad range of scales is required in order to simultaneously image the surface waves most affected by the bottom and those most affected by currents. The spatial field of view (FOV) must be several times the length of the longest waves to obtain reasonable spatial spectral estimates, thus the footprint must be hundreds of meters to 1 km or larger. The current-induced Doppler shift primarily affects waves that are less than 20 m in length, with shorter waves experiencing larger shifts, so the spatial resolution should be several meters or smaller. Also, since the scene is dynamic and typical cameras only capture images for a small fraction of the sampling interval, the temporal sampling must be fast enough to minimize aliasing in the temporal domain. For gravity waves that are 2 m and longer, the dispersion relation requires a sampling rate greater than 1.25 Hz to prevent aliasing of this type. Good estimates of the temporal frequencies of the waves require a dwell time that is several times the longest periods of the surface waves that are present, so dwell times of 30 s or more are needed. Thus, the pointing accuracy must be sufficient to maintain most of the imaged area within the FOV for the entire dwell. In addition, the data acquisition system must be able to handle the required data transfer rates and have sufficient data storage capacity for flight times of reasonable length. Large areas can be covered by looking out at moderate to small grazing angles from the aircraft. However, grazing angles that are too small distort the view of the waves, as noted previously, so moderate grazing angles (20°–30°) are preferred. Finally, the system was required to be small and lightweight enough to be installed on a single-engine aircraft and have the potential to be moved to a UAV at some later date. The design specifications that resulted from these requirements are summarized in Table 1.

The system components were chosen based on these requirements and are illustrated in the block diagram in Fig. 1. The camera has a 1024 × 1024 pixel CCD array that can be sampled at a frame rate of up to 8 Hz. Although the system was specified to sample at 2 Hz, higher rates provide the potential for noise reduction, though with a corresponding penalty in data storage requirements. The 12-bit quantization of the camera provides sufficient sensitivity to resolve ocean wave contrast while maintaining the generally brighter coast on the digitizer scale. This is a problem for cameras with more limited dynamic range, such as video cameras. The imaging lens on the camera is anamorphic, with an FOV of 18.6° in azimuth and 9.4° in elevation. The two-to-one aspect ratio approximately accounts for the projection of the FOV onto a level geodetic surface from

TABLE 1. AROSS operating specifications.

Characteristic	Value
Spatial resolution	2 m
Field of view	$18.6^\circ \times 9.4^\circ$
Footprint	$2 \text{ km} \times 2 \text{ km}$
Image sampling rate	2, 4 or 8 Hz
Dwell time	$\geq 30 \text{ s}$
CCD array	$1024 \times 1024 \text{ pixels}$
Data transfer rate	up to 18 MB s^{-1}
Data storage capability	$\geq 3 \text{ h}$ total imaging time at 2 Hz
Relative pointing stability: azimuth	$160 \mu\text{rad}$
Relative pointing stability: elevation	$320 \mu\text{rad}$
Absolute pointing stability: azimuth	1.6 mrad
Absolute pointing stability: elevation	3.2 mrad
Power consumption	$\leq 1 \text{ kW}$
Weight	$\leq 150 \text{ kg}$

the nominal grazing angle of approximately 30° relative to the ocean surface. The remaining perspective distortion imposed by the viewing geometry is corrected during the mapping of the imagery to a level geodetic coordinate system prior to Fourier analysis (see section 3). With the nominal viewing geometry given by an aircraft altitude of 2.8 km and a ground distance to the target of 5.6 km, this camera provides spatial resolution of 2 m (pixel)^{-1} and a $2 \text{ km} \times 2 \text{ km}$ FOV. A 100-nm optical bandpass filter centered at 600 nm restricts the response of the camera to the red to green region of the spectrum.

The camera was fitted with a motorized iris controller, and a combination of the exposure time and the iris setting is used to control the exposure of the CCD. Exposure can be controlled manually by either or both of these, and an automatic exposure mode is provided as well. In this mode, the average intensity of 100×100 pixels in the center of the array is monitored and used to drive a software control system that computes an appropriate exposure time and iris setting that adjusts as the scene changes (particularly with respect to sun glitter). To minimize blurring due to aircraft motion, exposure times are limited to a maximum of 20 ms. Tests with longer exposure times confirmed this limit, as longer times lead to apparent image motion, which becomes particularly evident in the portion of the scene containing some land.

As described above, the system was required to stare at a commanded target with useful precision for the indicated dwell, regardless of the orientation of the aircraft. Commercial positioners, which provide motion compensation and can be mounted on moving platforms such as fixed-wing aircraft and helicopters, are available. An external turret-type positioner currently used on the Predator surveillance UAV (Mulford 1994) was modified for this application. This positioner is a 4-axis gimballed turret that houses the camera/lens system, and it provides unlimited motion in azimuth and $+20^\circ$ to -90° in elevation. It was mounted to the underside of the payload bay in the nose of a modified Cessna 337

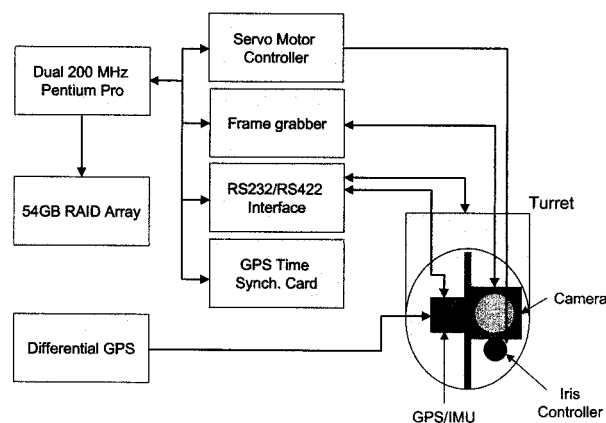


FIG. 1. Block diagram of the turret and camera system.

Skymaster, which is operated by the Naval Postgraduate School (NPS) Center for Interdisciplinary Remotely Piloted Aircraft Studies (CIRPAS). The pusher engine in this aircraft was replaced by a higher power engine, and the tractor engine was removed and replaced by a long nose and instrument payload bay. Consequently, it is called the *Pelican* (Bluth et al. 1996). The payload bay also contains support electronics, the system data acquisition/control computer, the data storage medium, and a GPS antenna. Figure 2 is a photograph of the camera and turret as mounted on the *Pelican* nose cone.

A small, affordable, readily available GPS/IMU was chosen with the pointing stability specifications listed in Table 1. The camera and GPS/IMU were bore-sighted in the laboratory to determine the relative orientation of their frames of reference. The GPS/IMU was placed in the turret (rather than on the airframe) to enhance turret system pointing accuracy. An order of magnitude improvement in pointing accuracy is possible in comparison to the approach in which a GPS/IMU mounted on the aircraft frame measures the aircraft attitude, and the turret attitude is provided by its internal feedback potentiometers. Differential GPS corrections are obtained from either the Coast Guard differential GPS service or the Omnistar commercial subscription satellite service and provided to the GPS/IMU via RS232 through the turret slip ring. The GPS/IMU integrates the differential GPS data with the inertial measurements using a Kalman filter and provides the turret location and attitude to the computer controller at a rate of 10 Hz. The computer uses these values along with the requested target GPS location to derive an angular error signal. The error signal drives a proportional and integral control system that outputs an angular rate signal to the turret drive motors at a rate of 50 Hz. In this design, no information is required from the aircraft navigation system, and the sensor operates autonomously. The specifications for this GPS/IMU result in absolute turret position and attitude errors of approximately 3 m in turret location and 2–4 rad in elevation and azimuth.

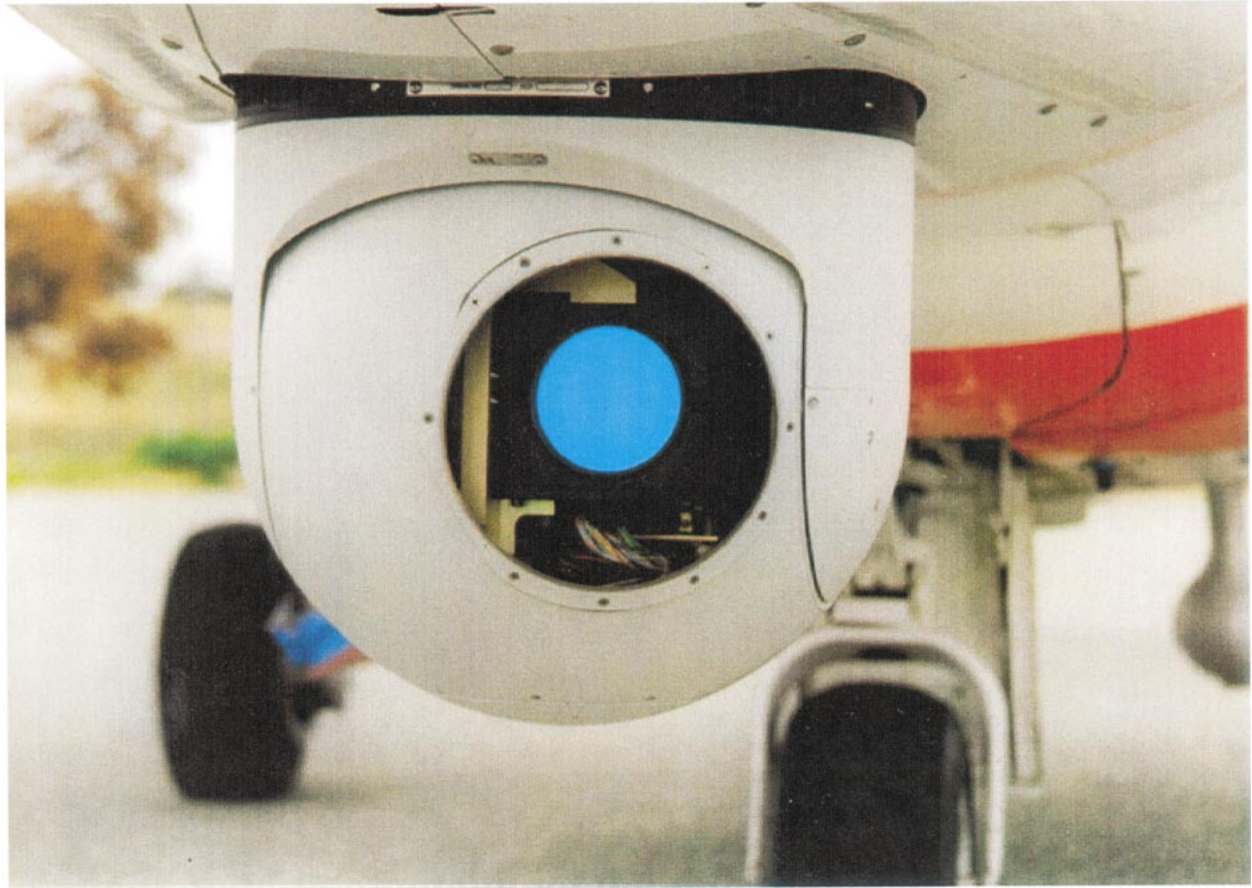


FIG. 2. Close-up photo of camera and turret as mounted on the nose cone of the *Pelican* aircraft.

At the intended range and grazing angle, these errors translate to absolute pointing accuracy of about 20 m and interframe accuracy of better than 5 m in both range and azimuth. For the intended application, these values meet the requirements that most of the imaged area is retained in continuous view over the dwell, and the jitter is small. Most importantly, the accuracy of the mapping can be improved by postprocessing when there is a stationary target in the FOV. Thus, the plan for data collection was to have such a target in the imagery over the entire dwell, either some part of the coast or a buoy or other offshore target having reasonably small motion.

The camera and GPS/IMU are interfaced through the turret slip ring to the data acquisition and turret control computer and the GPS antenna. The computer is a rack-mounted dual 2000 MHz Pentium Pro running Windows NT. The PCI bus shares a frame grabber, a GPS time card, a redundant array of independent disks (RAID) controller, and an RS422/RS232 serial port expander. The RAID system is composed of three 18 GB drives, formatted in RAID type 0, providing over 50 GB of data storage capacity. Data transfer from the RAID controller to the drives is via three independent ultrawide

SCSI channels, with a throughput rate of 30 MB s^{-1} , although only 18 MB s^{-1} are required for the maximum frame capture rate of 8 Hz. The RAID capacity is large enough to record continuously for over 3 h at the 2-Hz rate. The aircraft alternator provides 28 V of power for the system. On startup, AROSS draws approximately 20 A and, in steady state operation, the nominal current draw is 12 A. The total weight of the system is 150 kg.

A graphical user interface provides system control, image display, and operational status information regarding important elements of the system to an onboard operator who sits in the copilot's seat in this aircraft. A number of operational modes are available. The primary mode of operation is automated; the operator selects the GPS coordinates of a predetermined target, and the computer automatically points the turret at the selected coordinates. Manual control, in which the operator manually commands the turret attitude, is typically used at takeoff and landing to position the viewing port up into the payload bay, protecting the glass port from damage. It can also be used to manually point the camera system to an intended target during data acquisition as well. The pointing accuracies noted previously are defined only for the automated mode of operation.

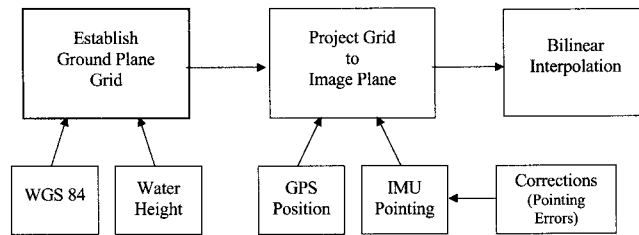


FIG. 3. Block diagram of the mapping software.

3. Data collection and processing

In order to achieve the required spatial resolution, FOV, and grazing angle, a nominal data collection flight geometry was defined. A typical data collection run consists of one orbit of the target location at the nominal aircraft altitude of 2.8 km, ground range of 5.6 km, and resulting grazing angle of about 27° . At a typical aircraft speed of 130 kt (67 m s^{-1}), a complete orbit of the target requires approximately 8 min, and results in ~ 1000 frames of data at the nominal 2-Hz rate. A segment of this dataset is then selected for processing, taking care to avoid segments with excessive sun glitter.

The selected image data are mapped by transforming them to a uniform rectilinear grid at the World Geodetic System 1984 vertical level of the mean ocean surface, using laboratory-derived optical distortion data for the lens and the camera attitude and position data from the GPS/IMU. This processing technique is summarized in the block diagram in Fig. 3. As mentioned in the previous section, with no external information, the absolute pointing accuracy is about 20 m rms at a nominal range of 6 km, and smooth drift in the aim point of up to $\sim 60 \mu\text{rad s}^{-1}$ has been observed over a minute of dwell, due to errors in the IMU data. At the nominal viewing geometry, this corresponds to a scene drift in the mapped imagery of up to 40 cm s^{-1} , a value that is typical of currents in coastal regions. Although this motion does not significantly affect the extracted bathymetry, it shifts the location of the dispersion surface in the same way that a mean surface current would. Ground control points (GCPs) may be used if they are available to improve the mapping accuracy, and they are necessary to obtain accurate currents when such drifts are present. For example, at familiar locations like the U.S. Army Corps of Engineers Field Research Facility (FRF) at Duck, North Carolina, we have placed a number of precisely located targets that can be identified in the imagery and used to correct for pointing drift or jitter. Alternatively, visible stationary features with unknown coordinates can be used in the same way to reduce unintended motion of the mapped scene.

Further processing of the mapped data consists of frame-by-frame mean normalization, a 3D detrend, and an 80% cosine window to reduce the effects of spectral leakage. The data are then Fourier transformed in time and two spatial dimensions to obtain the 3D ω - κ spectrum. This is typically done for subimages of 64, 128,

or 256 pixels on a side and for 64, 128, or 256 frames. Each resulting spectral estimate is averaged over three adjacent values in both wavenumber and frequency. The result for even a single subpatch is reasonably smooth, as shown in the example discussed below.

4. Results

A sample mapped AROSS image of the area around FRF is shown in Fig. 4 along with a photograph of the same area, collected with an aerial survey mapping camera within a day or two. They are essentially identical except for obvious human activities, such as cars on the road, and items, such as the research tower and other topographic features, that are at heights that are significantly different from the vertical level to which the data have been mapped. Since the mapping algorithm assumes that the scene is at a constant altitude, tall features suffer uncorrected perspective distortion in the resulting mapped image.

Figure 5 is a sample mapped AROSS image from Monterey Bay, near Santa Cruz, California, that shows obvious wind waves (H_{mo} was about 1 m), kelp beds, boat wakes, and a small section of coastline. The black edges result from the rotation of the image into geographic coordinates and correction for perspective distortion. The center 256×256 pixel portion of this image was enlarged to give a better view of the wave structure. These data were collected on 8 July 1999 using the nominal collection geometry described previously and target coordinates of $36^\circ 56.65' \text{N}$, $122^\circ 1.65' \text{W}$. A 1-min segment of data starting at 21 09:45 UTC was chosen for processing. Although this particular dataset was taken at 8 Hz, the segment to be processed was downsampled to 2 Hz by selecting every fourth frame. The center 256×256 pixel \times 128 frame data cube was Fourier transformed, and the 2D ω - κ slice through the 3D spectrum in the direction of the wind waves, slightly toward the north of east, is shown in Fig. 6, plotted as a function of $f = \omega/2\pi$ (Hz) and $k = \kappa/2\pi$ (cycles m^{-1}). This spectrum illustrates several interesting phenomena. The waves are distributed more or less along the theoretical deep water dispersion surface that intersects this spectral plane, which is shown as the smooth curved line on the plot. There is swell of about 100-m wavelength and wind waves from this length almost all the way down to the spatial Nyquist of 4-m wavelength. The higher frequency waves were originally rotated from the theoretical dispersion surface by an IMU pointing drift of about $60 \mu\text{rad s}^{-1}$, which resulted in scene motion of 40 cm s^{-1} . This drift was removed using the kelp beds, which appear as dark areas in the upper part of Fig. 5 as GCPs. Since the kelp beds are stationary over the dwell and are at sea level, they were used to remap the images to stationary spatial coordinates. Most of the energy of the resulting spectrum falls on the theoretical dispersion surface. The spectrum is narrow enough compared with the observed rotation caused by the image



FIG. 4. Comparison of (a) an aerial survey photo of the area around the Army Corps of FRF in Duck, NC, and (b) an AROSS image after mapping to geographic coordinates on a uniform rectilinear grid. These images are about 1 km across.

drift that any additional rotation of the dispersion surface due to currents could be estimated to a precision of about 5 cm s^{-1} or better. This leads to the conclusion that there were no significant surface currents in this location at the time these data were collected.

A second observation is that the low-frequency wave energy is slightly shifted from the theoretical deep water dispersion surface, even after the drift has been removed, suggesting that the water depth was shallow enough that the longer swell was affected. The water would have to be less than about 20–30-m depth to be able to discern such a change in location of the spectrum for these 100-m wavelengths. The local nautical chart shows the water depth to be about 18 m in this vicinity, which is consistent with these data. As stated in the introduction of this paper, the identification, and estimation of such changes in location of the energy is a primary objective for the development of this system, but further evaluation of the ability to retrieve depths and currents is beyond the scope of this paper. Another interesting feature is the strong, narrow peak in power on the upwind side of the spectrum at a frequency, f , of $\sim 0.33 \text{ Hz}$ with a wavelength of about 17 m ($k = 0.06 \text{ m}^{-1}$). This is due to the presence in the imagery of a Kelvin wake generated by the boat at the far left of the image in Fig. 5 and propagating toward the west-southwest, whereas the primary wind waves were propagating to the east-northeast. Thus, the energy appears on the opposite side of the wavenumber axis. Finally, there is an apparent ridge of energy that is propagating in the direction of the wind waves but at a much lower speed of about 2 m s^{-1} . (Speed on this spectral plot is calculated by drawing a line through the origin, and the

value of the speed is simply the slope of the line or the ratio ω / κ .) This feature is most likely a nonlinear effect that could be due to several physical wave or imaging mechanisms, such as relief distortion or *sidebands* (Walker 1994, p. 394), but its source has not been specifically identified.

Two 2D κ_x – κ_y slices at constant temporal frequencies ($f = 0.1$ and 0.4 Hz) through the same 3D spectrum are shown in Fig. 7, plotted vs k_x and k_y in cycles m^{-1} , along with the smooth circle, which is the intersection of the theoretical dispersion surface with these constant-frequency planes. The linear waves are propagating on or near the dispersion surface, both with and against the wind, and the nonlinear features can be seen moving at slower speeds in the general wind direction; this is particularly apparent in the lower frequency slice. The bright spots near 17-m wavelength ($k = 0.06 \text{ m}^{-1}$) in both constant frequency slices are due to spectral leakage in the frequency direction of the Kelvin wave pattern. These waves are traveling on the correct dispersion surface, but they appear at the wrong locations in these plots because of the leakage.

These spectral results were recalculated for several values of the subpatch image size and temporal dwell, as noted above, and the resulting thickness of the surface in the 3D space depended upon the spectral resolution in the expected manner. An algorithm has been developed, which fits the theoretical dispersion function to the spectral surface by varying the values of the depth and current, and this now is being applied to data collected on shoaling waves as they approached the surf at FRF during the recent Shoaling Wave Experiment (SHOWEX) exercise, and results will be reported in due

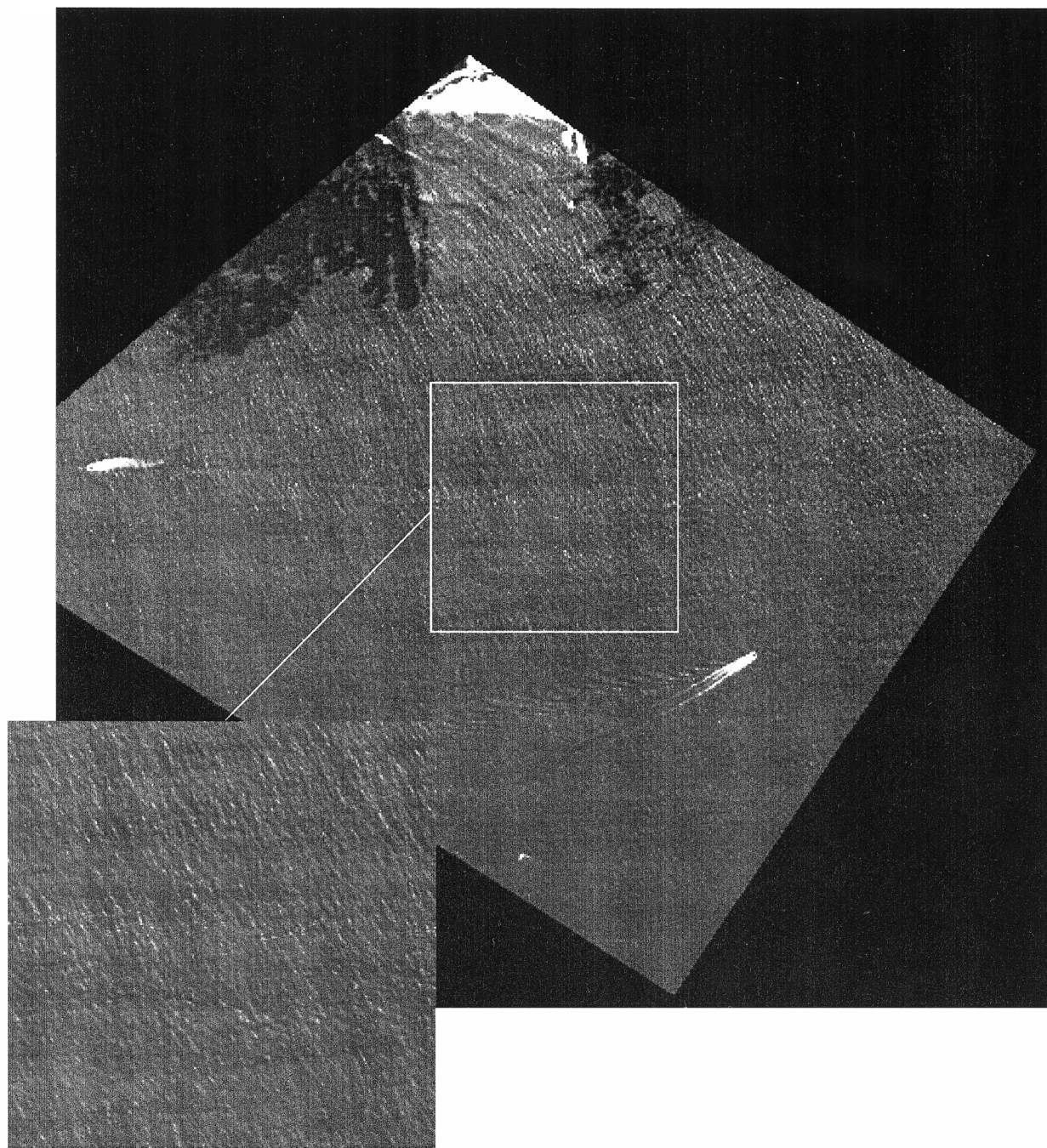


FIG. 5. Mapped data frame of Monterey Bay showing boat Kelvin wakes and kelp beds (top). The central portion, which was used to calculate the 3D spectrum (Figs. 6 and 7), has been enlarged to better illustrate the wave information it contains. This image is about 2 km across.

course. The thickness of this spectral surface clearly will affect the accuracy of retrievals of water depth or currents, so we expect to find that the larger the subpatch size and the longer the dwell, the more accurate the results. Finally, the ratio of the power on the spectral surface to the nearby noise level, the signal to noise ratio or *wave contrast*, is 20 or 30 db in all the data we

have collected and processed to date. This excellent dynamic range for this application, as the waves are very well resolved in relation to any competing noise. This is far superior to any space-time radar measurements that have been collected using systems mounted on towers on the beach that have been published to date (cf. Young et al. 1985.) However, the actual power num-

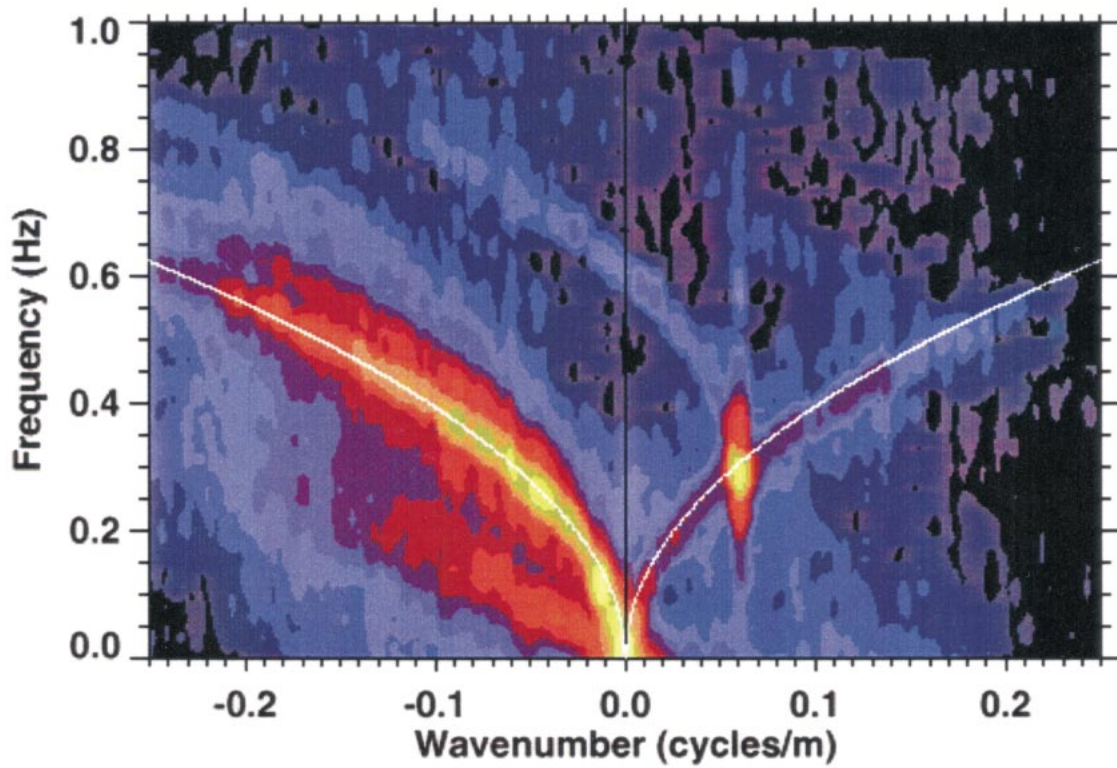


FIG. 6. The 2D frequency–wavenumber slice through the 3D spectrum in the direction of the wind. The solid white line is the linear deep water dispersion relation.

bers in these spectra represent radiance units, as noted previously, and without information on the background sky gradient, the spectral distribution of power cannot be directly translated into units of wave slope spectra.

5. Summary

In summary, AROSS performs as designed, providing useful data that are collected at modest grazing angles with

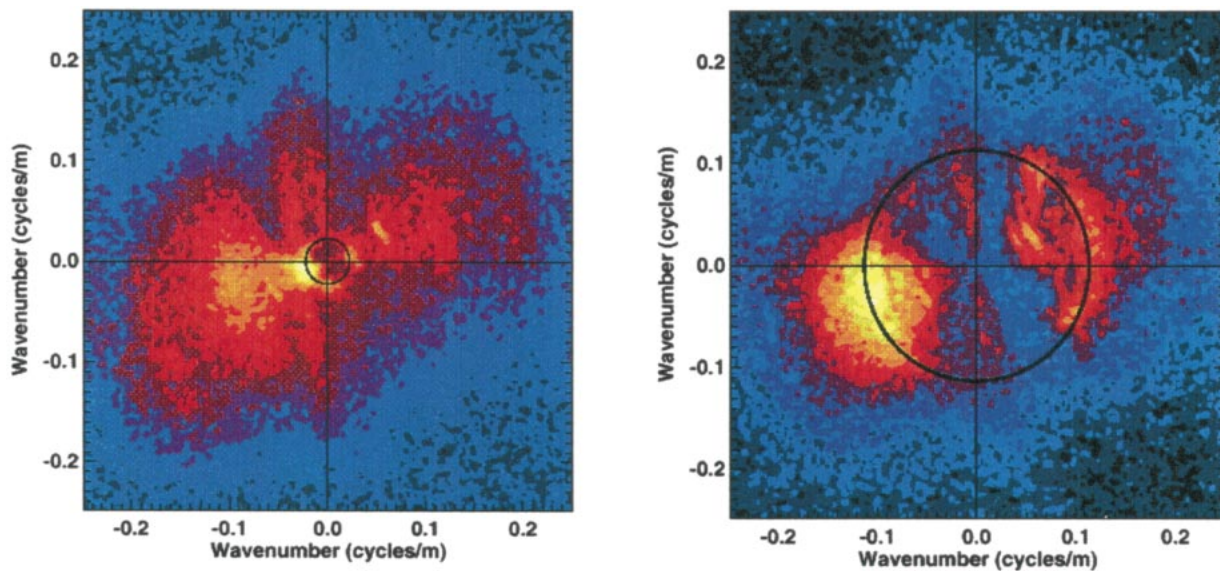


FIG. 7. Constant temporal frequency slices after remapping at (a) the swell frequency of 0.1 Hz, and (b) 0.4 Hz showing wind waves. The circles indicate the intersection of the dispersion surface with each constant-frequency plane.

enough control that they can be mapped successfully to a level geodetic surface. Imagery of ocean waves has been collected and mapped to the mean water surface, and 3D frequency–wavenumber spectra have been computed. These spectra exhibit a number of interesting features, including wind waves and swell propagating on the theoretical dispersion surface both with and against the wind direction, and other nonlinear features that are propagating at slower speed than the linear waves. In some of the results processed to date, the system pointing control drifts at slow speed ($\leq 60 \mu\text{rad s}^{-1}$) due to drift in the GPS/IMU, resulting in apparent scene motion of up to 40 cm s^{-1} at the nominal viewing geometry. This motion could be confused with water currents, but the image drift can be removed by remapping the data to stationary coastal features, eliminating the ambiguity. The spectra are very well resolved, and appear to be adequate for use in extracting information on water depth and currents in shallow water. Experiments have been planned and recently conducted as part of the SHOWEX located at the FRF near Duck, North Carolina, to examine the precision with which these quantities can be extracted, and preliminary results are promising. In addition, the spectra exhibit excellent directional resolution, as one fully expects with an optical system, and detailed comparisons with in situ directional wave buoys and the bottom pressure array at FRF are planned.

Acknowledgments. This development was supported by an Office of Naval Research Small Business Innovative Research Project under contract N00014-97-C-0309. Bob Bluth of CIRPAS made the necessary arrangements for use of a bare Predator turret, and he and the personnel of the NPS CIRPAS were particularly cooperative and helpful in the integration of our system with the Pelican aircraft and with flight testing and operations.

REFERENCES

- Barber, N. F., 1949: A diffraction analysis of a photograph of the sea. *Nature*, **164**, 485.
- Bierwirth, P. N., T. J. Lee, and R. V. Burne, 1993: Shallow sea-floor reflectance and water depth derived by unmixing multispectral imagery. *Photogramm. Eng. Remote Sens.*, **59**, 331–338.
- Bluth, R. T., P. A. Durkee, J. H. Seinfeld, R. C. Flagan, and L. M. Russell, 1996: Center for Interdisciplinary Remotely-Piloted Aircraft Studies (CIRPAS). *Bull. Amer. Meteor. Soc.*, **77**, 2691–2699.
- Chapman, R. D., and G. B. Irani, 1981: Errors in estimating slope spectra from wave images. *Appl. Opt.*, **20**, 3645–3652.
- Dugan, J. P., 1997: Bathymetry measurements from long range airborne imaging systems. *Proc. Fourth Int. Conf. on Remote Sensing for Marine and Coastal Environments*, Vol. I, Orlando, FL, Environmental Research Institute of Michigan, 451–457.
- , H. H. Suzukawa, C. P. Forsyth, and M. S. Farber, 1996: Ocean wave dispersion measured with airborne IR imaging system. *IEEE Trans. Geosci. Remote Sens.*, **34**, 1282–1284.
- Holland, K. T., R. A. Holman, and T. C. Lippmann, 1997: Practical use of video imagery in nearshore oceanographic field studies. *IEEE Trans. J. Oceanic Eng.*, **22**, 81–92.
- Kasevich, R. S., C. H. Tang, and S. W. Henriksen, 1972: Analysis and optical processing of sea photographs for energy spectra. *IEEE Trans. Geosci. Remote Sens.*, **10**, 51–58.
- Lillycrop, W. J., L. E. Parsons, and J. L. Irish, 1996: Development and operation of the SHOALS airborne lidar hydrographic system. *Laser Remote Sensing of Natural Waters: From Theory to Practice, Selected Papers*, V. I. Feigels and Y. I. Kopilevich, Eds., Vol. 2694, International Society for Optical Engineering, 26–37.
- Lippmann, T. C., and R. A. Holman, 1989: Quantification of sand bar morphology: A video technique based on wave dissipation. *J. Geophys. Res.*, **94**, 995–1011.
- Lubard, S. C., J. E. Krimmel, L. R. Thebaud, D. D. Evans, and O. H. Shemdin, 1980: Optical image and laser slope meter inter-comparison of high-frequency waves. *J. Geophys. Res.*, **85**, 4996–5002.
- Lundahl, A. C., 1948: Underwater depth determination by aerial photography. *Photogramm. Eng.*, **14**, 454–462.
- Mulford, L., 1994: Skyball: The eyes for Predator. *Unmanned Syst.*, **12**, 30–31.
- Seiwel, H. R., 1947: Military oceanography in World War II. *Mil. Eng.*, **39**, 202–210.
- Stilwell, D., 1969: Directional energy spectra of the sea from photographs. *J. Geophys. Res.*, **74**, 1974–1986.
- Walker, R. E., 1994: *Marine Light Field Statistics*. Wiley, 675 pp.
- Williams, J. Z., and J. P. Dugan, 1997: Bathymetry measurements using electro-optical remote sensing. *Proc. Fourth Int. Conf. on Remote Sensing for Marine and Coastal Environments*, Vol. II, Orlando, FL, Environmental Research Institute of Michigan, 572–581.
- Young, I. R., W. Rosenthal, and F. Ziemer, 1985: A three-dimensional analysis of marine radar images for the determination of ocean wave directionality and surface currents. *J. Geophys. Res.*, **90**, 1049–1059.